Detection of Atherosclerotic Plaque from Optical Coherence Tomography Images Using Texture-Based Segmentation

Ammu Prakash, M.Sc., PhD Student, Department Electrical and Computer Engineering[1];
Mark D. Hewko, M.Eng., B.Sc.Eng., Research Council Officer[2]; Adjunct Professor,
Department of Biosystems Engineering[1];
Michael Sowa, PhD, Principal Research Officer and Group Leader, Medical Devices Portfolio[2];
Sherif S. Sherif, PhD, Associate Professor, Department Electrical and Computer Engineering[1]

[1]University of Manitoba, 75 Chancellor's Circle, Winnipeg, R3T 5V6, Manitoba, Canada;
[2]Institute for Biodiagnostics, National Research Council Canada, 435 Ellice Avenue, Winnipeg, Manitoba,
 R3B 1Y6, Canada

Detection of atherosclerotic plaque from optical coherence tomography (OCT) images by visual inspection is difficult. We developed a texture based segmentation method to identify atherosclerotic plaque automatically from OCT images without any reliance on visual inspection. Our method involves extraction of texture statistical features (spatial gray level dependence matrix method), application of an unsupervised clustering algorithm (K-means) on these features, and mapping of the clustered regions: background, plaque, vascular tissue and an OCT degraded signal region in feature-space, back to the actual image. We verified the validity of our results by visual comparison to photographs of the vascular tissue with atherosclerotic plaque that were used to generate our OCT images. Our method could be potentially used in clinical studies in OCT imaging of atherosclerotic plaque.

Key words: optical coherence tomography; tissue texture; unsupervised clustering; atherosclerosis.

Introduction

Atherosclerosis as cause of cardiovascular diseases. Cardiovascular diseases continue to be a leading cause of morbidity and mortality for both genders around the globe [1]. Atherosclerosis is considered to be the underlying cause of the majority of cardiovascular diseases [2]. Atherosclerosis is a series of immuno-inflammatory events in the arterial wall that can lead to the development of lipid laden lesions. Plaques may appear with a wide range of morphological and anatomical features. The risk for cardiovascular complications is strongly linked to the phenotypical characteristics of the plaque. Histologically it has been determined that plaques with thin collagen caps are more likely associated with acute thrombosis due to cap rupture or erosion [3]. The lipid burden retained within the plaque portends its lethal potential [4]. Despite the importance of the plaque structure and biochemical composition, there are few clinical techniques that provide this information, *in vivo*. Angiographic imaging methods are extremely good at finding flow-limiting stenotic lesions while computed tomography can accurately detect calcified lesions. The advent of intravascular ultrasound (IVUS) and intravascular optical coherence tomography (IVOCT) with their increased spatial resolution, enhanced contrast of soft tissues and volumetric imaging capability has opened the possibility of studying plaque structure, in-detail, in patients undergoing intravascular imaging. In particular, OCT with its very high resolution and ability to contrast structural proteins such as collagen from lipids seems well suited to detect plaque risk stratification. Reliable detection of plaque and characterization of its structure with OCT and their prophylactic treatment at the time of intervention could potentially translate into an improved long term outcome for the patient.

Imaging of plaque using optical coherence tomography. OCT is analogous to ultrasound imaging which uses sound waves to create images with resolution of the order of tens of microns. OCT systems create images using back-reflection of infrared light instead of sound waves, which allows approximately 10 times higher imaging resolution than ultrasound at shallower penetration depths. The axial and lateral resolutions of OCT are approximately 5–10 and 15–30 µm respectively.

Many biomedical imaging modalities have been utilized to detect plaque pathology. These modalities include IVUS [5–7], computed tomography [8–10], and magnetic resonance imaging [11, 12]. IVOCT is a minimally invasive microscopic imaging technology that has been developed for the identification of plaque [13–20]. The first investigation of IVOCT demonstrated its potential to perform micron scale tomographic imaging of the internal microstructure of *in vitro* atherosclerotic plaques [21]. Several features of OCT make it attractive for intravascular imaging, e.g., high imaging resolution, small size of fiber-based imaging probes and the availability of image processing techniques to extract diagnostic information from the resulting images.

Corresponding author: Sherif S. Sherif, e-mail: Sherif.Sherif@umanitoba.ca

Studies have shown that using texture analysis, it may be possible for OCT to better distinguish different arterial structures in OCT images [22–28]. There exists literature on atherosclerotic plaque segmentation using IVUS [29, 30], computed tomography [31] and magnetic resonance imaging [32]. However, OCT offers a combination of micron-scale morphological imaging with penetration depths of 1–3 mm which makes it particularly attractive among other imaging modalities. A study was conducted comparing OCT–IVUS image pairs obtained from different patients [33]. In all cases it was found IVOCT observations were more consistent than IVUS. On the basis of these findings, IVOCT has emerged as a promising imaging modality for extracting plaque diagnostic information.

Texture segmentation of OCT images. Texture segmentation is the process of identifying different regions within an image based on the different regions' texture. The properties of the texture of an image can be measured by its histogram and its statistical moments. There are different methods to extract texture features using statistical methods. There exists a large body of literature on texture feature extraction methods for example, spatial gray level dependent matrix (SGLDM) method, grey level difference method, grey level run length method, and power spectral method. However a study comparing these methods has concluded that the SGLDM method is the most powerful texture feature extraction method [34]. Recent studies have shown that texture analysis can be useful in segmenting similar appearing tissue types based on its speckle features [35–38].

In this paper we describe a new method to segment regions of atherosclerotic plaque and vascular tissue on OCT images using SGLDM.

Experimental setup

Animal model. We used myocardial infarction prone Watanabe heritable hyperlipidemic rabbits, referred
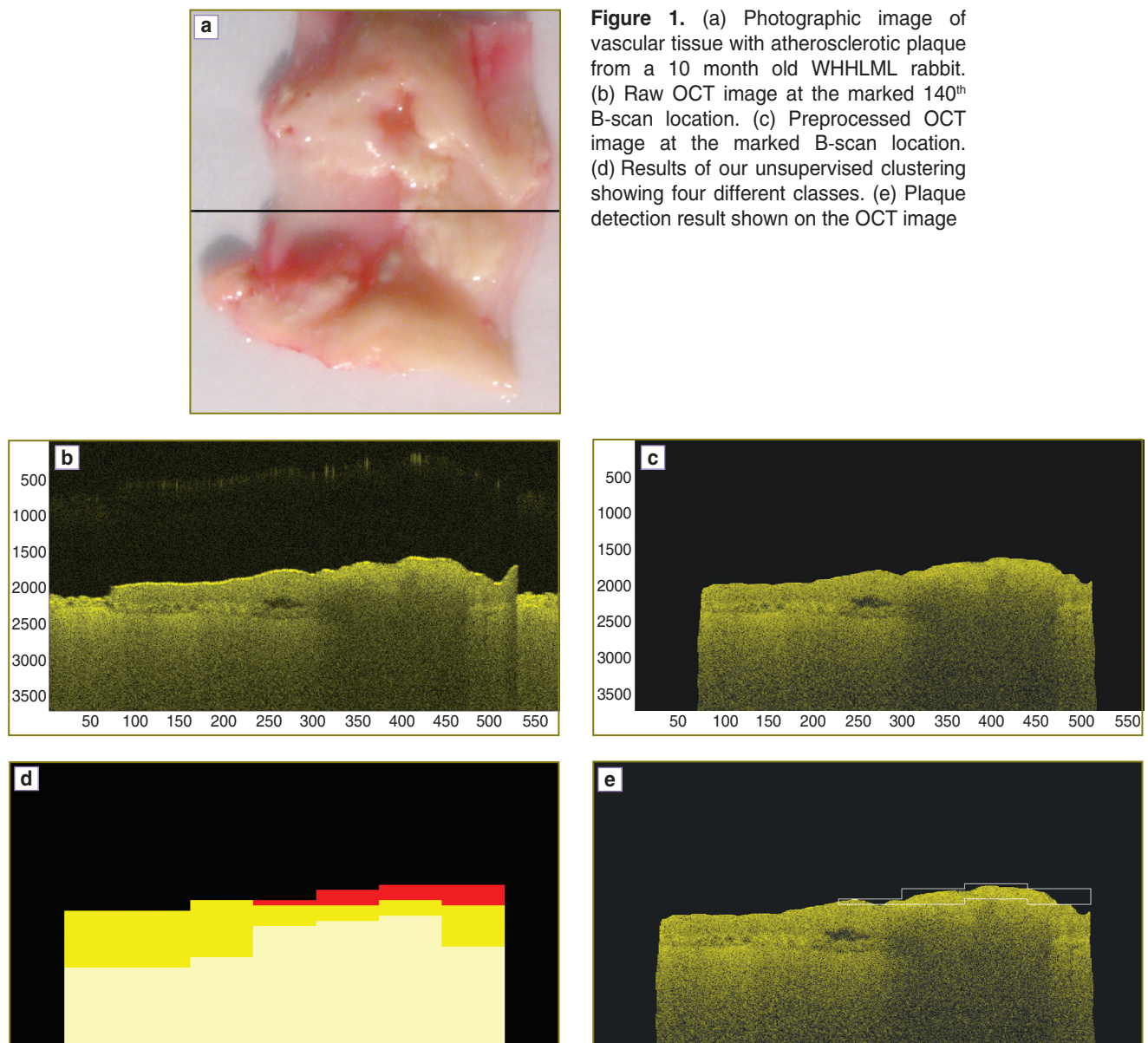
Figure 1. (a) Photographic image of vascular tissue with atherosclerotic plaque from a 10 month old WHHLML rabbit. (b) Raw OCT image at the marked 140th B-scan location. (c) Preprocessed OCT image at the marked B-scan location. (d) Results of our unsupervised clustering showing four different classes. (e) Plaque detection result shown on the OCT image

Ammu Prakash, Mark D. Hewko, Michael Sowa, Sherif S. Sherif

as WHHLMI rabbits [39] to obtain samples of vascular tissues with atherosclerotic plaque. Arterial sample from two WHHLMI rabbits aged 10 and 19 months at different locations were obtained (Figure 1–3 (a)). Arterial segments of tissue starting from the ascending aorta to the external iliac artery were excised from all specimens and subdivided into 20–30 mm long sections. This study was approved by the local animal care committee at Institute for Biodiagnostics, National Research Council Canada (Winnipeg, Manitoba).

OCT imaging of vascular tissue sample. We used a swept-source OCT (SS-OCT) system to image vascular tissue sample from WHHLMI rabbits. The SS-OCT system employed a central wavelength of 1310 nm with a sweep rate and spectral range of 30 kHz and 110 nm respectively. Our SS-OCT unit was configured as a Mach–Zehnder interferometer with balanced optical detection.

Methods

Image preprocessing. To achieve a uniform distribution of intensities and to improve contrast we performed image normalization on each raw OCT vascular image file. This was performed by a min–max normalization, defined as

$$Preprocessed\ image = \frac{\min(Image)}{\max(Image) - \min(Image)} \times 255. \quad (1)$$

To improve the image quality, we also performed image segmentation using automatic thresholding technique. Our raw OCT image contained 4 regions: *air*, *plaque*, *vascular tissue* and an *OCT degraded signal region*. This automatic thresholding technique is based on Ostu method [40], it computes a global threshold value. This value is further used to convert the intensity image into binary image which isolates object of interest from its background, leaving out two regions as foreground and background. An optimal

Figure 2. (a) Photographic image of vascular tissue with atherosclerotic plaque from a 10 month old WHHLML rabbit. (b) Raw OCT image at the marked 290th B-scan location. (c) Preprocessed OCT image at the marked B-scan location. (d) Results of our unsupervised clustering showing four different classes. (e) Plaque detection result shown on the OCT image
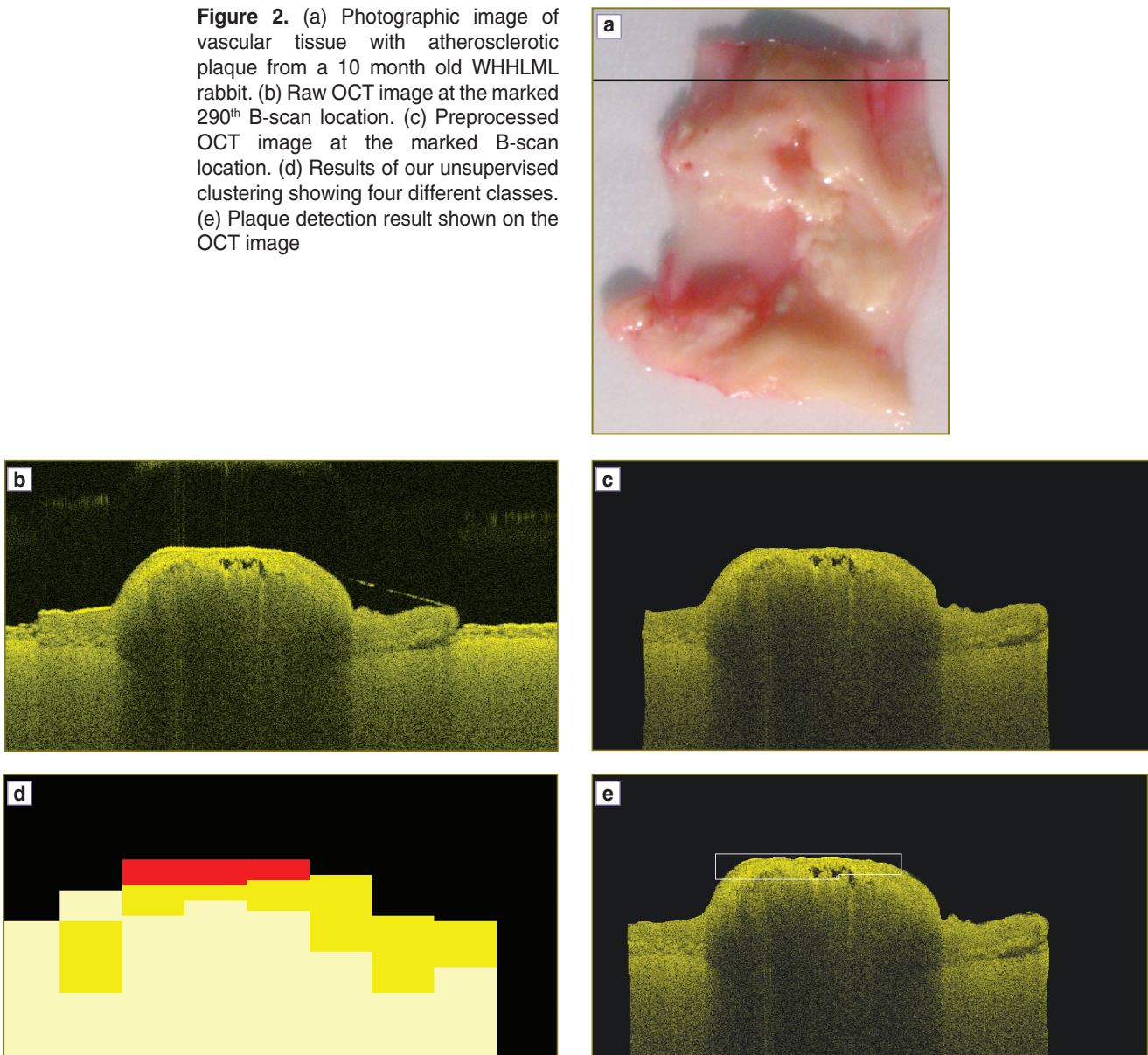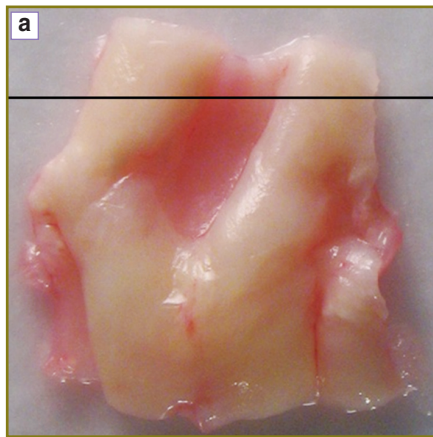
Figure 3. (a) Photographic image of vascular tissue with atherosclerotic plaque from a 19 month old WHHLML rabbit. (b) Raw OCT image at the marked 180th B-scan location. (c) Preprocessed OCT image at the marked B-scan location. (d) Results of our unsupervised clustering showing four different classes. (e) Plaque detection result shown on the OCT image
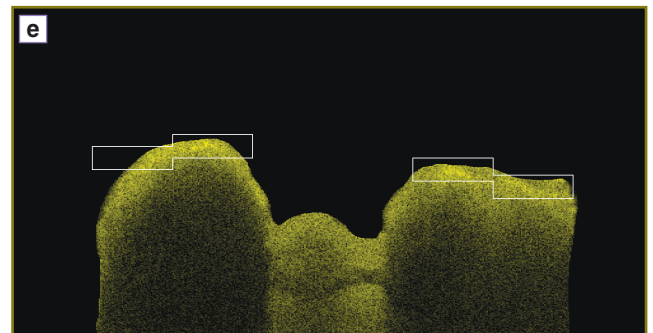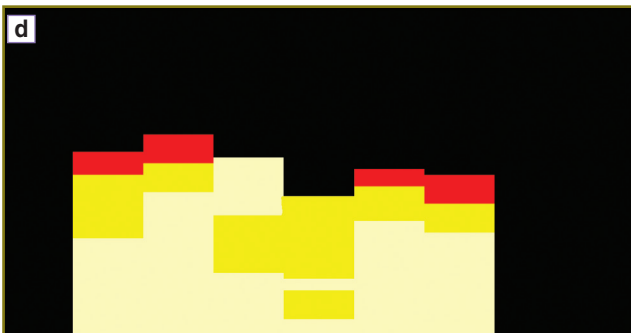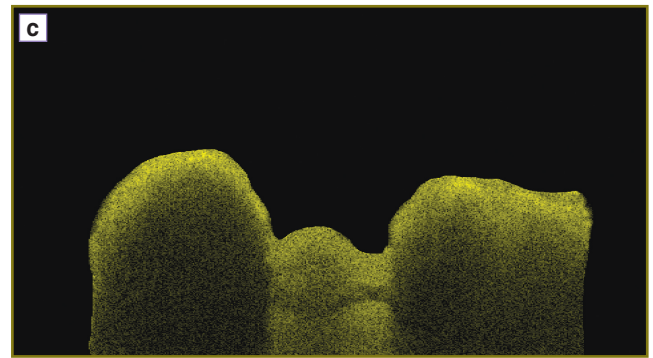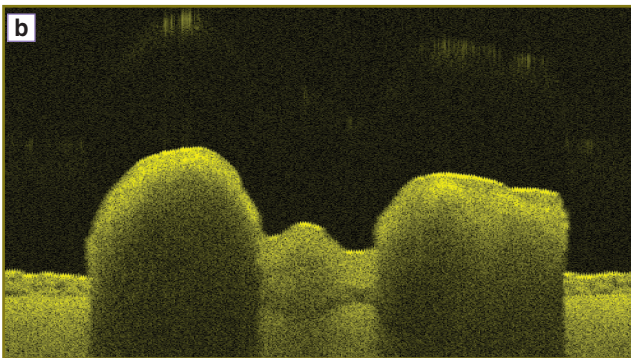
threshold value is selected to maximize the intraclass variance of thresholded black and white pixels. We employed MATLAB function graythreshold to carry out this process. Finally, by multiplying this binary image with the original raw OCT image, replaced air with black pixels and remaining as tissue region containing plaque and healthy tissue. We also used imfreehand tool in MATLAB to remove the water layer and paper tissue on which the tissue sample was placed while imaging.

Feature extraction and feature normalization. We extracted texture features from our processed OCT vascular images using SGLDM method. Features derived from the SGLDM method have been widely used for classification of tissue images [41–44]. The SGLDM method determines the probability of occurrence of specific grey levels as a function of pixel position in an image. This method makes use of co-occurrence or spatial dependence matrices which are texture transforms of the original image. These spatial dependence matrices are based on an estimate of second-

order joint conditional probability density functions P $(i, j; d, \theta)$ [45]. These probability density functions P $(i, j; d, \theta)$ measure the probability that two pixels, located at sample distance d and direction θ, have grey levels i and j. To detect the atherosclerotic plaque, we extracted 9 texture features in two directions: $\theta = 0°$ and $90°$ which resulted in total 18 features with $d = 1$ and from these spatial dependence matrices directly. These SGLDM features are shown in the Table. Even though these textural image features contain information about textural image characteristics of an image, it is difficult to identify which specific textural image characteristic is represented by each of these features [46]. However few of the features have visual definition for example $F1$ (angular second moment) is the measure of smoothness of the image. The less smooth a region is, the lower its angular second moment. $F8$ (entropy) is the measure of randomness in an image. For smooth images, the value of entropy will be low.

An important decision is to choose the size of the image

Ammu Prakash, Mark D. Hewko, Michael Sowa, Sherif S. Sherif

window over which SGLDM matrices are calculated. Small windows may not have enough pixels to accurately capture the texture of underlying tissue while too large window may contain tissue of grossly different texture. We tried different window sizes and found the window size of 63×63 pixels led the best results for plaque segmentation from other regions.

The scale of the texture features has different dynamic ranges. To ensure that all the features have similar influence on performance of our method, we normalized the entire texture feature vector. Each texture feature vector was normalized as:

$$\hat{x} = \frac{x - \bar{x}}{\sigma}, \qquad (2)$$

where x is the raw feature vector, $\bar{x}$ is the mean of all entries of x and σ is corresponding standard deviation.

Image clustering algorithm. After texture feature normalization, we carried out atherosclerotic plaque detection on OCT images using K-means clustering algorithm [47, 48], which is popular clustering technique due to its simplicity and fast convergence. We applied the K-means clustering algorithm on the texture feature space to segment the *background*, *plaque*, *vascular tissue* and the *OCT degraded signal region* and then we mapped the segmented features back to original image.

The K-means algorithm requires four parameters: 1) number of segments, 2) a distance metric, 3) initial location of segments' centroids, and 4) a criterion to stop iteration.

As our preprocessed OCT images consist of *background*, *plaque*, *vascular tissue*, and an *OCT degraded signal region*, we selected the number of segments, K=4. The knowledge of 4 segments was available as a prior knowledge from the actual photographic images. We defined distance between each segment by a Euclidean distance and initialized segment centroids randomly. For each texture feature vector, we calculated Euclidean distance from the segment centroid. Our criterion to stop iteration was, if the texture feature vector was not closest to its own segment centroid, it was to be shifted into the closest cluster. Otherwise, the feature vector was not shifted. The process continued until convergence was achieved.

Image segmentation results and discussion. Our results show the ability of our method to detect atherosclerotic plaque automatically from OCT images. On comparing our segmented OCT with photographic image, it is clear that there is a close match between the plaque locations (Figures 1–3 (a) and (e)). To the unaided eye, it is difficult to differentiate the plaque from the remaining tissue regions of the raw OCT image.

Mathematical expression of SGLDM features

Feature number	Feature name	Formula
F1, F10	Angular second moment at orientations (θ=0°, θ=90°)	$\sum_i \sum_j (P(i, j)^2)$
F2, F11	Variance at orientations (θ=0°, θ=90°)	$\sum_i \sum_j (i-\mu)^2 P(i, j)$
F3, F12	Sum average at angles(θ=0°, θ=90°)	$\sum_{i=0}^{2(N_g-1)} i P_{x+y}(i)$, where x and y are the coordinates of an entry in SGLDM matrix and $P_{x+y}(i)$ is the probability of SGLDM matrix coordinates summing to $x+y$
F4, F13	Sum variance at orientations (θ=0°, θ=90°)	$\sum_{i=0}^{2N_g-2} (i-F_5)^2 P_{x+y}(i)$
F5, F14	Sum entropy at orientations (θ=0°, θ=90°)	$-\sum_{i=0}^{2N_g-2} P_{x+y}(i) \log\{P_{x+y}(i)\}$
F6, F15	Entropy at orientations (θ=0⁰, θ=90⁰)	$-\sum_i \sum_j P(i, j) \log P(i, j)$
F7, F16	Difference variance at orientations (θ=0°, θ=90°)	$-\sum_{i=0}^{N_g-1} (i-F_5)^2 P_{x-y}(i)$
F8, F17	Difference entropy at orientations (θ=0°, θ=90°)	$-\sum_{i=0}^{N_g-1} P_{x-y}(i) \log P_{x-y}(i)$
F9, F18	Information measure II of correlation at orientations (θ=0°, θ=90°)	$\sqrt{1 - \exp(-2(H_{xy}^2 - H_{xy}))}$, where $H_{xy} = -\sum_i \sum_j p(i, j) \log(p(i, j))$, $H_{xy}^2 = -\sum_j \sum_i P_x(i) P_y(j) \log(P_x(i) P_y(j))$

N o t e: $P(i, j)$ is the ith and j^{th} entry in SGLDM matrix. $P_x(i)$ is the marginal probability of ith entry. N_g is the number of gray levels in the images. $P_y(i)$ is the marginal probability of jth entry.

K-means is considered as the standard unsupervised clustering method due to its simplicity and efficiency. The main goal of this algorithm is to partition data points into different clusters based on its similarities. It also requires user to specify the total number of clusters. In this work, we clustered data points based on its similar statistical properties from the OCT textural image. We assumed the total number of clusters which is 4 as prior information from the photographic vascular images. In future work, we aim to investigate different clustering algorithms which will not require the user to set a priori so as to improve the sensitivity. We also aim to reduce our number of features by employing feature reduction techniques and thereby extend our method to handle real time applications.

Conclusions. In this work, we implemented an automated unsupervised clustering algorithm to detect the plaque region from OCT vascular images of arterial tissue in an automatic way. This approach mainly incorporates SGLDM method and K-means clustering algorithm. Our methodology extracts the texture features of the OCT vascular images based on their statistics rather than their visible structure. Our results show excellent matching with actual photographs of vascular tissue with atherosclerotic plaque. Our plaque detection approach is a first step towards using the texture of OCT images to differentiate plaque phenotypes. Linking textural characteristics of lesions to the structural integrity of plaques could have significant impact to help diagnosis and manage atherosclerosis.

Conflict of Interests. The authors have no conflict of interests to disclose.

References

1. Hoyert D.L., Xu J. Deaths: preliminary data for 2011. *Nat Vital Stat Rep* 2012; 61(6): 1–51.

2. Lloyd-Jones D., Adams R.J., Brown T.M., Carnethon M., Dai S., De Simone G., Ferguson T.B., Ford E., Furie K., Gillespie C., Go A., Greenlund K., Haase N., Hailpern S., Ho P.M., Howard V., Kissela B., Kittner S., Lackland D., Lisabeth L., Marelli A., McDermott M.M., Meigs J., Mozaffarian D., Mussolino M., Nichol G., Roger V.L., Rosamond W., Sacco R., Sorlie P., Stafford R., Thom T., Wasserthiel-Smoller S., Wong N.D., Wylie-Rosett J. Heart disease and stroke statistics — 2010 update a report from the American Heart Association. *Circulation* 2010; 121(7): e46–e215, http://dx.doi.org/10.1161/circulationaha.109.192667.

3. Burke A.P., Farb A., Malcom G.T., Liang Y., Smialek J., Virmani R. Coronary risk factors and plaque morphology in men with coronary disease who died suddenly. *N Engl J Med* 1997; 336(18): 1276–1282, http://dx.doi.org/10.1056/NEJM199705013361802.

4. Fuster V., Moreno P.R., Fayad Z.A., Corti R., Badimon J.J. Atherothrombosis and high-risk plaque: part I: evolving concepts. *J Am Coll Cardiol* 2005; 46(6): 937–954, http://dx.doi.org/10.1016/j.jacc.2005.03.074.

5. Takayama T., Hiro T., Yamagishi M., Daida H., Hirayama A., Saito S., Yamaguchi T., Matsuzaki M.; The COSMOS investigators. Effect of rosuvastatin on coronary atheroma in stable coronary artery disease: multicenter coronary atherosclerosis study measuring effects of rosuvastatin using intravascular ultrasound in Japanese subjects (COSMOS). *Cir J* 2009; 73(11): 2110–2117, http://dx.doi.org/10.1253/circj.CJ-09-0358.

6. Kubo T., Maehara A., Mintz G.S., Doi H., Tsujita K., Choi S.-Y., Katoh O., Nasu K., Koenig A., Pieper M., Rogers J.H., Wijns W., Böse D., Margolis M.P., Moses J.W., Stone G.W., Leon M.B. The dynamic nature of coronary artery lesion morphology assessed by serial virtual histology intravascular ultrasound tissue characterization. *J Am Coll Cardiol* 2010; 55(15): 1590–1597, http://dx.doi.org/10.1016/j.jacc.2009.07.078.

7. Lee C.-H., Tai B.-C., Soon C.-Y., Low A.F., Poh K.-K., Yeo T.-C., Lim G.-H., Yip J., Omar A.R., Teo S.-G., Tan H.-C. New set of intravascular ultrasound-derived anatomic criteria for defining functionally significant stenoses in small coronary arteries (results from intravascular ultrasound diagnostic evaluation of atherosclerosis in Singapore [IDEAS] study). *Am J Cardiol* 2010; 105(10): 1378–1384, http://dx.doi.org/10.1016/j.amjcard.2010.01.002.

8. Arbab-Zadeh A., Miller J.M., Rochitte C.E., Dewey M., Niinuma H., Gottlieb I., Paul N., Clouse M.E., Shapiro E.P., Hoe J., Lardo A.C., Bush D.E., de Roos A., Cox C., Brinker J., Lima J.A.C. Diagnostic accuracy of computed tomography coronary angiography according to pre-test probability of coronary artery disease and severity of coronary arterial calcification: the CORE-64 (coronary artery evaluation using 64-row multidetector computed tomography angiography) international multicenter study. *J Am Coll Cardiol* 2012; 59(4): 379–387, http://dx.doi.org/10.1016/j.jacc.2011.06.079.

9. de Graaf F.R., Schuijf J.D., van Velzen J.E., Kroft L.J., de Roos A., Reiber J.H.C., Boersma E., Schalij M.J., Spanó F., Jukema J.W., van der Wall E.E., Bax J.J. Diagnostic accuracy of 320-row multidetector computed tomography coronary angiography in the non-invasive evaluation of significant coronary artery disease. *Eur Heart J* 2010; 31(15): 1908–1915, http://dx.doi.org/10.1093/eurheartj/ehp571.

10. Bamberg F., Sommer W.H., Hoffmann V., Achenbach S., Nikolaou K., Conen D., Reiser M.F., Hoffmann U., Becker C.R. Meta-analysis and systematic review of the long-term predictive value of assessment of coronary atherosclerosis by contrast-enhanced coronary computed tomography angiography. *J Am Coll Cardiol* 2011; 57(24): 2426–2436, http://dx.doi.org/10.1016/j.jacc.2010.12.043.

11. Underhill H.R., Hatsukami T.S., Fayad Z.A., Fuster V., Yuan C. MRI of carotid atherosclerosis: clinical implications and future directions. *Nat Rev Cardiol* 2010; 7(3): 165–173, http://dx.doi.org/10.1038/nrcardio.2009.246.

12. Kwee R.M., van Oostenbrugge R.J., Mess W.H., Prins M.H., van der Geest R.J., ter Berg J.W.M., Franke C.L., Korten A.G.G.C., Meems B.J., van Engelshoven J.M.A., Wildberger J.E., Kooi M.E. MRI of carotid atherosclerosis to identify TIA and stroke patients who are at risk of a recurrence. *J Magn Reson Imaging* 2013; 37(5): 1189–1194, http://dx.doi.org/10.1002/jmri.23918.

13. Bezerra H.G., Attizzani G.F., Sirbu V., Musumeci G., Lortkipanidze N., Fujino Y., Wang W., Nakamura S., Erglis A., Guagliumi G., Costa M.A. Optical coherence tomography versus intravascular ultrasound to evaluate coronary artery disease and percutaneous coronary intervention. *JACC Cardiovasc Interv* 2013; 6(3): 228–236, http://dx.doi.org/10.1016/j.jcin.2012.09.017.

14. Parodi G., Maehara A., Giuliani G., Kubo T., Mintz G.S., Migliorini A., Valenti R., Carrabba N., Antoniucci D. Optical

coherence tomography in unprotected left main coronary artery stenting. *EuroIntervention* 2010; 6(1): 94–99, http://dx.doi.org/10.4244/eijv6i1a14.

15. Foin N., Mari J.M., Davies J.E., Di Mario C., Girard M.J.A. Imaging of coronary artery plaques using contrast-enhanced optical coherence tomography. *Eur Heart J Cardiovasc Imaging* 2013; 14(1): 85, http://dx.doi.org/10.1093/ehjci/jes151.

16. Wang T., Wieser W., Springeling G., Beurskens R., Lancee C.T., Pfeiffer T., van der Steen A.F.W., Huber R., van Soest G. Intravascular optical coherence tomography imaging at 3200 frames per second. *Opt Lett* 2013; 38(10): 1715–1717, http://dx.doi.org/10.1364/OL.38.001715.

17. Gubarkova E.V., Kirillin M.Yu., Sergeeva E.A., Kiseleva E.B., Snopova L.B., Prodanets N.N., Sharabrin L.G., Shakhov E.B., Nemirova S.V., Gladkova N.D. Cross-polarization optical coherence tomography in evaluation of atherosclerotic plaque structure. *Sovremennye tehnologii v medicine* 2013; 5(4): 45–54.

18. van Soest G., Goderie T., Regar E., Koljenović S., van Leenders G.L.J.H., Gonzalo N., van Noorden S., Okamura T., Bouma B.E., Tearney G.J., Oosterhuis J.W., Serruys P.W., van der Steen A.F. Atherosclerotic tissue characterization in vivo by optical coherence tomography attenuation imaging. *J Biomed Opt* 2010; 15(1): 011105, http://dx.doi.org/10.1117/1.3280271.

19. Prati F., Regar E., Mintz G.S., Arbustini E., Di Mario C., Jang I.-K., Akasaka T., Costa M., Guagliumi G., Grube E., Ozaki Y., Pinto F., Serruys P.W.J. Expert review document on methodology, terminology, and clinical applications of optical coherence tomography: physical principles, methodology of image acquisition, and clinical application for assessment of coronary arteries and atherosclerosis. *Eur Heart J* 2010; 31(4): 401–415, http://dx.doi.org/10.1093/eurheartj/ehp433.

20. Li Q.-X., Fu Q.-Q., Shi S.-W., Wang Y.-F., Xie J.-J., Yu X., Cheng X., Liao Y.-H. Relationship between plasma inflammatory markers and plaque fibrous cap thickness determined by intravascular optical coherence tomography. *Heart* 2010; 96(3): 196–201, http://dx.doi.org/10.1136/hrt.2009.175455.

21. Brezinski M.E., Tearney G.J., Bouma B.E., Boppart S.A., Hee M.R., Swanson E.A., Southern J.F., Fujimoto J.G. Imaging of coronary artery microstructure (in vitro) with optical coherence tomography. *Am J Cardiol* 1996; 77(1): 92–93, http://dx.doi.org/10.1016/S0002-9149(97)89143-6.

22. Gossage K.W., Tkaczyk T.S., Rodriguez J.J., Barton J.K. Texture analysis of optical coherence tomography images: feasibility for tissue classification. *J Biomed Opt* 2003; 8(3): 570–575, http://dx.doi.org/10.1117/1.1577575.

23. Lindenmaier A.A., Conroy L., Farhat G., DaCosta R.S., Flueraru C., Vitkin I.A. Texture analysis of optical coherence tomography speckle for characterizing biological tissues in vivo. *Opt Lett* 2013; 38(8): 1280–1282, http://dx.doi.org/10.1364/OL.38.001280.

24. Quellec G., Lee K., Dolejsi M., Garvin M.K., Abràmoff M.D., Sonka M. Three-dimensional analysis of retinal layer texture: identification of fluid-filled regions in SD-OCT of the macula. *IEEE Trans Med Imaging* 2010; 29(6): 1321–1330, http://dx.doi.org/10.1109/TMI.2010.2047023.

25. Liu L., Gardecki J.A., Nadkarni S.K., Toussaint J.D., Yagi Y., Bouma B.E., Tearney G.J. Imaging the subcellular structure of human coronary atherosclerosis using micro-optical coherence tomography. *Nat Med* 2011; 17(8): 1010–1014, http://dx.doi.org/10.1038/nm.2409.

26. Takano M., Yamamoto M., Inami S., Murakami D., Ohba T., Seino Y., Mizuno K. Appearance of lipid-laden intima and neovascularization after implantation of bare-metal stents extended late-phase observation by intracoronary optical coherence tomography. *J Am Coll Cardiol* 2009; 55(1): 26–32, http://dx.doi.org/10.1016/j.jacc.2009.08.032.

27. Mizukoshi M., Imanishi T., Tanaka A., Kubo T., Liu Y., Takarada S., Kitabata H., Tanimoto T., Komukai K., Ishibashi K., Akasaka T. Clinical classification and plaque morphology determined by optical coherence tomography in unstable angina pectoris. *Am J Cardiol* 2010; 106(3): 323–328, http://dx.doi.org/10.1016/j.amjcard.2010.03.027.

28. Uemura S., Ishigami K., Soeda T., Okayama S., Sung J.H., Nakagawa H., Somekawa S., Takeda Y., Kawata H., Horii M., Saito Y. Thin-cap fibroatheroma and microchannel findings in optical coherence tomography correlate with subsequent progression of coronary atheromatous plaques. *Eur Heart J* 2012; 33(1): 78–85, http://dx.doi.org/10.1093/eurheartj/ehr284.

29. Hoogi A., Adam D., Hoffman A., Kerner H., Reisner S., Gaitini D. Carotid plaque vulnerability: quantification of neovascularization on contrast-enhanced ultrasound with histopathologic correlation. *AJR Am J Roentgenol* 2011; 196(2): 431–436, http://dx.doi.org/10.2214/AJR.10.4522.

30. Partovi S., Loebe M., Aschwanden M., Baldi T., Jäger K.A., Feinstein S.B., Staub D. Contrast-enhanced ultrasound for assessing carotid atherosclerotic plaque lesions. *AJR Am J Roentgenol* 2012; 198(1): W13–W19, http://dx.doi.org/10.2214/AJR.11.7312.

31. Vukadinovic D., Rozie S., van Gils M., van Walsum T., Manniesing R., van der Lugt A., Niessen W.J. Automated versus manual segmentation of atherosclerotic carotid plaque volume and components in CTA: associations with cardiovascular risk factors. *Int J Cardiovasc Imaging* 2012; 28(4): 877–887, http://dx.doi.org/10.1007/s10554-011-9890-6.

32. Morishige K., Kacher D.F., Libby P., Josephson L., Ganz P., Weissleder R., Aikawa M. High-resolution magnetic resonance imaging enhanced with superparamagnetic nanoparticles measures macrophage burden in atherosclerosis. *Circulation* 2010; 122(17): 1707–1715, http://dx.doi.org/10.1161/CIRCULATIONAHA.109.891804.

33. Jang I.-K., Bouma B.E., Kang D.-H., Park S.-J., Park S.-W., Seung K.-B., Choi K.-B., Shishkov M., Schlendorf K., Pomerantsev E., Houser S.L., Aretz H.T., Tearney G.J. Visualization of coronary atherosclerotic plaques in patients using optical coherence tomography: comparison with intravascular ultrasound. *J Am Coll Cardiol* 2002; 39(4): 604–609, http://dx.doi.org/10.1016/s0735-1097(01)01799-5.

34. Conners R.W., Harlow C.A. A theoretical comparison of texture algorithms. *IEEE Trans Pattern Anal Mach Intell* 1980; 2(3): 204–222, http://dx.doi.org/10.1109/tpami.1980.4767008.

35. Sullivan A.C., Hunt J.P., Oldenburg A.L. Fractal analysis for classification of breast carcinoma in optical coherence tomography. *J Biomed Opt* 2011; 16(6): 066010, http://dx.doi.org/10.1117/1.3590746.

36. Flueraru C., Popescu D.P., Mao Y., Chang S., Sowa M.G. Added soft tissue contrast using signal attenuation and the fractal dimension for optical coherence tomography images of porcine arterial tissue. *Phys Med Biol* 2010; 55(8): 2317–2331, http://dx.doi.org/10.1088/0031-9155/55/8/013.

37. Lindenmaier A.A., Conroy L., Farhat G., DaCosta R.S., Flueraru C., Vitkin I.A. Texture analysis of optical coherence tomography speckle for characterizing biological tissues in vivo.

Opt Lett 2013; 38(8): 1280–1282, http://dx.doi.org/10.1364/OL.38.001280.

38. Kirillin M.Y., Farhat G., Sergeeva E.A., Kolios M.C., Vitkin A. Speckle statistics in OCT images: Monte Carlo simulations and experimental studies. *Opt Lett* 2014; 39(12): 3472–3475, http://dx.doi.org/10.1364/OL.39.003472.

39. Kobayashi T., Ito T., Shiomi M. Roles of the WHHL rabbit in translational research on hypercholesterolemia and cardiovascular diseases. *J Biomed Biotechnol* 2011; 2011: 406473, http://dx.doi.org/10.1155/2011/406473.

40. Otsu N. A threshold selection method from gray-level histograms. *Automatica* 1975; 11(285–296): 23–27.

41. Yu H., Caldwell C., Mah K., Mozeg D. Coregistered FDG PET/CT-based textural characterization of head and neck cancer for radiation treatment planning. *IEEE Trans Med Imaging* 2009; 28(3): 374–383, http://dx.doi.org/10.1109/TMI.2008.2004425.

42. Subashini T.S., Ramalingam V., Palanivel S. Automated assessment of breast tissue density in digital mammograms. *Computer Vision and Image Understanding* 2010; 114(1): 33–43, http://dx.doi.org/10.1016/j.cviu.2009.09.009.

43. Moayedi F., Azimifar Z., Boostani R., Katebi S. Contourlet-based mammography mass classification using the SVM family. *Comput Biol Med* 2010; 40(4): 373–383, http://dx.doi.org/10.1016/j.compbiomed.2009.12.006.

44. Garcia-Allende P.B., Amygdalos I., Dhanapala H., Goldin R.D., Hanna G.B., Elson D.S. Morphological analysis of optical coherence tomography images for automated classification of gastrointestinal tissues. *Biomed Opt Express* 2011; 2(10): 2821–2836, http://dx.doi.org/10.1364/BOE.2.002821.

45. Haralick R.M., Shanmugam K., Dinstein I.H. Textural features for image classification. *IEEE Trans Syst Man Cybern* 1973; 6: 610–621, http://dx.doi.org/10.1109/tsmc.1973.4309314.

46. Nielsen B., Albregtsen F., Danielsen H.E. Low dimensional adaptive texture feature vectors from class distance and class difference matrices. *IEEE Trans Med Imaging* 2004; 23(1): 73–84, http://dx.doi.org/10.1109/TMI.2003.819923.

47. Jain A.K. Data clustering: 50 years beyond K-means. *Pattern Recognition Letters* 2010; 31(8): 651–666, http://dx.doi.org/10.1016/j.patrec.2009.09.011.

48. Kirby M., Lee A.M.D., Candido T., MacAulay C., Lane P., Lam S., Coxson H.O. Automated segmentation of porcine airway wall layers using optical coherence tomography: comparison with manual segmentation and histology. *Pros. SPIE, Endoscopic Microscopy IX; and Optical Techniques in Pulmonary Medicine* 2014; 8927: 89271D, http://dx.doi.org/10.1117/12.2040866.

Ammu Prakash, Mark D. Hewko, Michael Sowa, Sherif S. Sherif